Letter

Contacts and upstream modes explain the electron-hole asymmetry in the graphene quantum Hall regime

N. Moreau [1], B. Brun [1], S. Somanchi,[2] K. Watanabe [3], T. Taniguchi,[4] C. Stampfer,[2] and B. Hackens [1]

[1]*IMCN/NAPS, Université Catholique de Louvain (UCLouvain), B-1348 Louvain-la-Neuve, Belgium*
[2]*JARA-FIT and 2nd Institute of Physics - RWTH Aachen 52074, Germany*
[3]*Research Center for Functional Materials, National Institute for Materials Science, Namiki 305-0044, Japan*
[4]*International Center for Materials Nanoarchitectonics, National Institute for Materials Science, Namiki 305-0044, Japan*

Observations of electron-hole asymmetry in transport through graphene devices at high magnetic field challenge prevalent models of the graphene quantum Hall effect. Here we study this asymmetry both in conventional magnetotransport and in scanning gate microscopy maps measured in an encapsulated graphene constriction. We reveal that the presence of upstream modes and local doping in the vicinity of electrical contacts leads to a totally different picture of topological breakdown for electrons and holes, explaining the observed asymmetry.

Injecting and collecting charges in two-dimensional electronic systems (2DESs) through ohmic contacts look like easy tasks, with most models describing contacts as smooth extensions of the 2DES. However, in the quantum Hall (QH) regime, the topic is far from trivial as charge carriers flow in different topologically protected QH edge channels (QHECs). Indeed, good coupling of these channels with the contacts involves no backscattering of incoming QHECs and perfect equilibration in the injection of carriers in the different outgoing QHECs. Fulfilling these two criteria proves difficult because of the complex interface between the metallic contacts and the 2DES [1–3].

In the graphene QH regime, the situation is even more cumbersome for two reasons at the least. First, state-of-the-art QH devices rely on graphene encapsulation in hexagonal boron nitride (hBN) and on 1D line-contacts obtained by depositing metal on the flanks of the device [4]. Such abrupt metal-graphene contact was shown to potentially destroy electron-hole symmetry [5]. Second, different experimental results indicate that upstream (i.e., counterpropagating) QHECs can flow along device edges [6–11]. The origin of upstream modes is ascribed to a peculiar shape of the confining potential at the edges, leading to Landau levels (LLs) being crossed twice by the Fermi energy [12].

Two explanations were invoked for the latter potential profile: Either an inhomogeneous screening of the back gate potential, related to fringing fields [12–14], or impurities at device edges [8,11]. Both hypotheses lead to charge accumulation at device borders [15]. However, charge accumulation does not seem to be ubiquitous; recent spatially resolved investigations of QHECs in graphene devices equipped with graphite back-gate did not show any sign of upstream QHECs [16]. The conditions for the emergence of upstream modes are therefore still to be clarified.

Thanks to scanning gate microscopy (SGM), topological breakdown of the QH effect has recently been shown to originate from the coupling of up- and downstream QHECs along the very same edge in this material [8,10]. In particular, we showed that the coupling is achieved through the localized states of antidots located along the edges [10]. Importantly, the latter SGM experiments have essentially focused on hole-type charge carriers and evidence for the same mechanisms for electron-type charge carriers remains elusive.

In this Letter, we combine transport and SGM with tight-binding simulations to study the topological breakdown of graphene QHECs in the case of electrons and holes. Our results reveal that contacts lead to a different spatial configuration of upstream QHECs for both types of charge carriers. This asymmetry is at the origin of distinct mechanisms causing a topological breakdown on the electron and hole sides.

The studied sample, depicted in Fig. 1(a), consists in a monolayer of graphene encapsulated between two hBN flakes [17] (see Supplemental Material [18], section S1). The longitudinal resistance R_{xx} is measured via line contacts made of gold deposited on a thin adhesion layer of chromium [4]. Inherently to this contact layout, they overlap the heterostructure. Charge-carrier density is varied using a back gate voltage V_{bg} and a magnetic field B is applied perpendicularly to the graphene plane. We furthermore use a sharp metallic SGM tip, biased at a voltage V_{tip} to change locally the charge-carrier density.

A fan diagram is presented in Fig. 1(b). The white stripes correspond to vanishing R_{xx} and indicate that QHECs are topologically protected, so that charge carriers backscattering is forbidden. Interestingly, the filling factors positions obtained by fitting these regions (blue dashed lines) do not correspond to the theoretical values obtained from a capacitance model (white dashed lines). It suggests a discrepancy between the bulk and the edge filling factor (see Supplemental Material [18], section S2). Furthermore, at low positive V_{bg} and above $B = 4\,\text{T}$, R_{xx} exhibits extremely large and irregular fluctuations. Such an asymmetric and perturbed behavior has
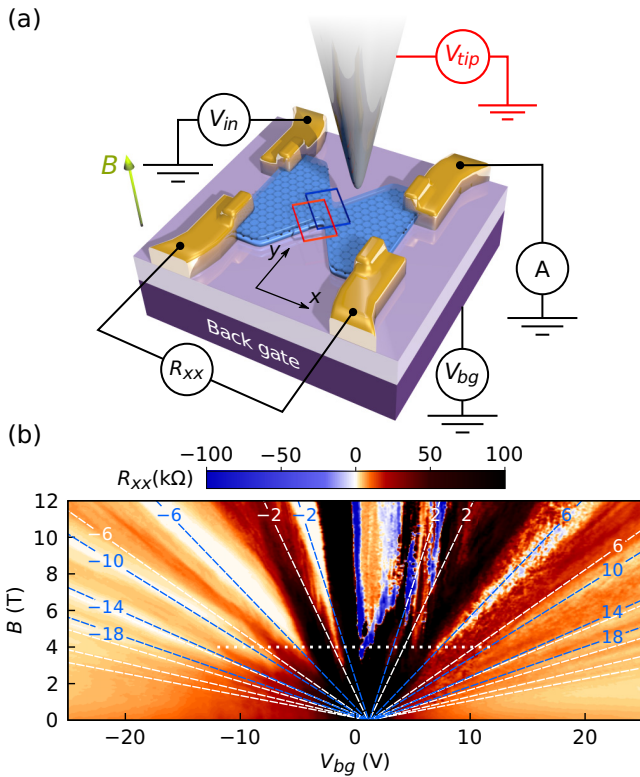
FIG. 1. (a) Artist view of the experimental setup. (b) R_{xx} map as a function of V_{bg} and B. The blue lines indicate the positions of the filling factors $\nu = \pm(4n + 2)$ obtained by a fit of the $R_{xx} = 0$ regions, and the white lines indicate the filling factors obtained using a theoretical capacitance model.

FIG. 2. (a) R_{xx} as a function of V_{bg} at $B = 4\,\text{T}$ [white dotted line in Fig. 1(b)]. The blue dashed lines indicate the positions of the filling factors $\nu = \pm(4n + 2)$. (b–d) SGM maps obtained in the vicinity of the constriction for holes (b) and electrons (c, d) (see also Supplemental Material, section S4). The scan area is depicted in Fig. 1(a) with a red rectangle for (b) and (c) and with a dark blue one for (d). The V_{bg} values are indicated with arrows in (a) and $V_{tip} = 0.5$ V in (b) and (c) and 1.5 V in (d). For holes, SGM contrast appears centered on the sample edge (purple arrow) as well as in the center of the constriction, whereas it is located exclusively at the center of the constriction for electrons (green arrows).

already been reported in Ref. [19] and is relatively common in the case of encapsulated graphene devices. In order to stand at the verge of this regime, we limit our measurements to $B = 4\,\text{T}$ (see Supplemental Material [18], section S3, and Refs. [20,21] therein) for the remainder of this paper. R_{xx} as a function of V_{bg} is shown in Fig. 2(a) for this value of magnetic field.

SGM maps, obtained by recording R_{xx} as a function of the tip position, reveal precious information on the origin of the coupling between QHECs. The tip perturbation locally tunes the coupling and, hence, the backscattering between QHECs [8,10,21–24]. In turn, this leads to concentric fringes of R_{xx} (local maxima or minima) in the SGM map, centered on the spot where the coupling occurs. As shown in Fig. 2(b), SGM contrasts are located along edges for holes. It is coherent with former studies that ascribed these signatures to the presence of upstream QHECs along the same edge, coupled with the downstream modes flowing closer to the edge [8,10]. As detailed in Ref. [10] and in the Supplemental Material [18], section S4, there is no qualitative difference in SGM contrast between images recorded close to and far from the integer filling factor, except in the number of sets of concentric circles. The reason for this absence of difference lies in the presence of counterpropagating edge states. When such states govern transport, it is not the bulk filling factor that plays the main role, but rather the filling factor of the edge region between counterpropagating states, as detailed hereafter.
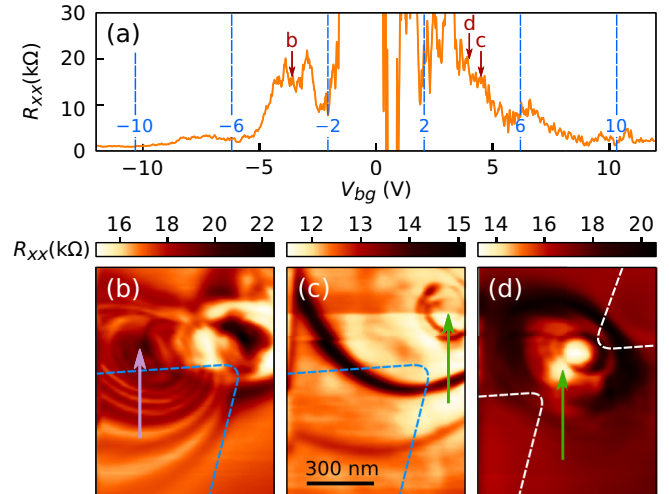
For electrons, however, SGM contrast is centered only in the constriction region, as indicated with SGM fringes with higher R_{xx} in Fig. 2(c) and with spots of lower R_{xx} in Fig. 2(d). Contrary to the hole case, no contrast is found centered on the edges of the device. It is noteworthy that similar signatures have been found in SGM experiments on classical semiconductor-based 2DESs [22,23], where there is no upstream QHEC. In these systems, topological breakdown was assigned to the presence of an antidot located in the vicinity of the constriction and coupling the QHECs running at the opposite device edges.

As a first hypothesis to account for electron-hole asymmetry, one could speculate that upstream QHECs only exist for holes. Impurities and defects along the borders could in this case favor hole accumulation and induce such charge asymmetry, as proposed in Refs. [8,11] (referred to hereafter as the "impurity model"). While our data cannot undoubtedly discard this scenario, the impurity model alone fails to yield a full picture of QHECs in graphene in regard to other experimental results reported in the literature [6] (see Supplemental Material [18], section S5). On the other hand, the mainstream theory, namely, the inhomogeneous screening of the backgate potential (the fringing field model), predicts the emergence of upstream QHECs both for holes and for electrons and consequently an apparent charge symmetry. In the following, we show that electron-hole asymmetry can also be explained in the fringing field model framework.

In the model that we develop hereafter, we assume that charge carriers accumulate along the edges in the same way on the electron and hole sides. The bending of energy bands
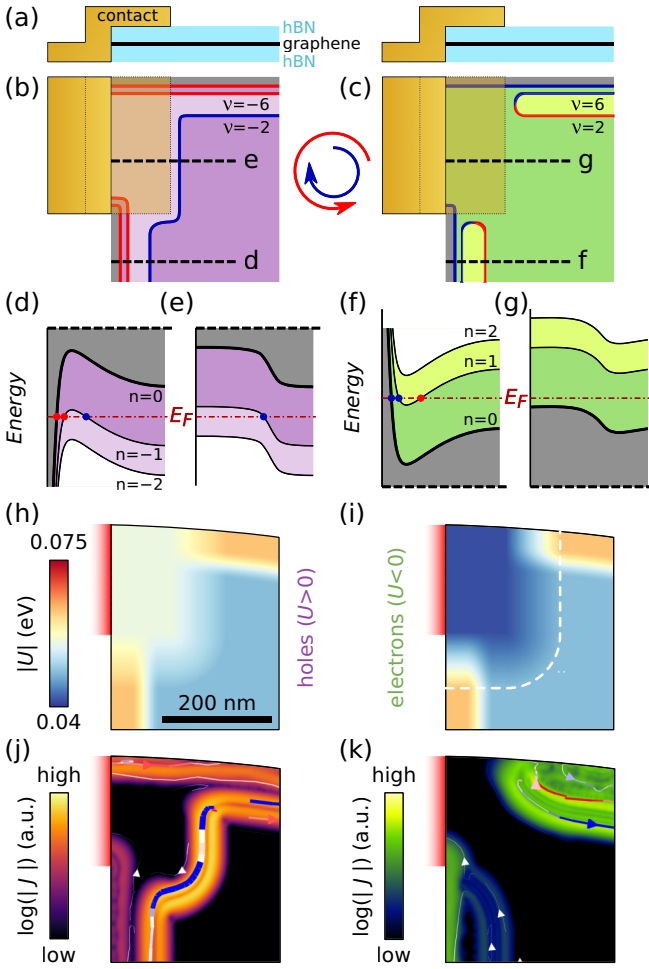
FIG. 3. (a) Side view of the device (schematic) in the vicinity of one of the contacts. (b, c) Top view of one of the sample corner, around the contact. Due to the increase of charge-carrier density at the device borders, upstream QHECs run along the edges (clockwise in blue and counterclockwise in red). If the contacts dope graphene with holes, the inner (clockwise) QHEC for holes circumvent the contact area (b), whereas the inner (counterclockwise) QHEC for electrons is merged with the nearest external (clockwise) QHEC (c). (d–g) Evolution of the potential (thick line) and the three first LLs along the black dashed lines in (b) and (c). QHECs appear where LLs cross the Fermi energy (red dashed line). (h, i) Absolute value of the onsite potential landscape $|U|$ used for the tight-binding simulations for holes with $V_{\mathrm{bg}} = -2.4\,\mathrm{V}$ (h) and electrons with $V_{\mathrm{bg}} = 2.4\,\mathrm{V}$ (i). The semi-infinite leads in the simulated system are depicted in red. (j, k) Current density maps obtained from tight-binding calculations for holes (j) and electrons (k).

leads in both cases to the presence of upstream QHECs. In this scenario, electron-hole asymmetry originates from the contacts. In particular, the difference of work function between graphene and chromium, forming the adhesion layer of contacts, yields a hole-type doping below the metallic regions overlapping the stack illustrated in Fig. 3(a). The work function-induced difference of the potential can be approximated by [25,26]

$$\Delta\phi = \frac{\sqrt{1 + 2\alpha e |W_{\mathrm{Cr}} - W_{\mathrm{G}}|} - 1}{\alpha}, \quad (1)$$

where $W_{\mathrm{Cr}} = 4.5\,\mathrm{eV}$ [27] (note that W_{Cr} depends on crystal orientations as discussed in the Supplemental Material [18], section S7, and Refs. [27–29] therein) and $W_{\mathrm{G}} = 4.48\,\mathrm{eV}$ [25] are the work functions of chromium and graphene, respectively, and $\alpha = 2e^2 t_{\mathrm{hBN}}/(\epsilon_{\mathrm{hBN}}\pi\hbar^2 v_F^2)$ with $t_{\mathrm{hBN}} \sim 20\,\mathrm{nm}$ the vertical distance between graphene and the overlapping metal, $2 < \epsilon_{\mathrm{hBN}} < 4$ the hBN permittivity, and $v_F \sim 10^6\,\mathrm{m/s}$ the Fermi velocity of graphene. With these data, we find $6 < \Delta\phi < 8\,\mathrm{meV}$. As a result, charge-carrier density is larger below the overlapping metal, with respect to the bulk, when the bulk is doped with holes, whereas it is smaller for an electron-doped bulk.

In the QH regime, this modulation of charge-carrier density has an important influence on the QHECs spatial configuration in the vicinity of the contacts, which differs for holes and electrons, as illustrated in Figs. 3(b) and 3(c). In this schematic, upstream QHECs flow along the edges where one of the bent LLs crosses twice the Fermi energy. This is illustrated in Figs. 3(d) and 3(f) for holes and electrons, respectively, using a schematic drawing of the potential profile close to device edges. However, this picture is no longer valid around and below the contacts pads, i.e., in the doped orange-shaded region in Figs. 3(b) and 3(c). For holes, the inner (clockwise) QHEC circumvent the contact zone, due to the increase of holes density [Fig. 3(e)]. For electrons, the lower charge density close to the contacts [Fig. 3(g)] leads to the merging of the inner (counterclockwise) with the closest clockwise QHECs [Fig. 3(c)]. These QHECs are therefore perfectly equilibrated.

To go beyond the above-described qualitative model, we performed tight-binding simulations using the KWANT package [30] (see Supplemental Material [18], section S8, and Ref. [31] therein). Maps of the absolute value of the on-site potential around the contacts are shown in Fig. 3(h) for holes and in Fig. 3(i) for electrons. They feature an increase of charge-carrier density along the edges, proportional to the bulk density, in addition to a constant positive offset energy $\Delta E = 7\,\mathrm{meV}$ [Eq. (1)] around the contacts. The resulting current density maps are presented in Figs. 3(j) and 3(k). The QHECs are visible in lighter tones and match the qualitative picture of Figs. 3(b) and 3(c).

We now consider the entire sample to examine the consequences of these different QHECs spatial configurations at the contacts for holes and electrons and the relationship with the experimental data of Fig. 2. For holes (left side of Fig. 4), it appears that the inner QHEC (blue) forms a closed loop, as illustrated in Fig. 4(a). In the absence of coupling with the outer QHECs (red), this loop is topologically equivalent to a localized state in QH theory since it is not directly coupled with contacts and should not influence transport. The effective filling factor of the system is, therefore, given by the region outside the loop (here $\nu = -6$ in light purple). To observe the topological breakdown of QHECs, holes running along one of the sample edges should be backscattered to the opposite edge. This can only be achieved by coupling the upstream QHEC loop both on the upper and on the lower sides of the sample, for example, at locations pinpointed by concentric black circles in Fig. 4(a). The SGM contrast highlighted along the sample edge in Fig. 2(b) is therefore the signature of one of the two coupling spots between upstream QHECs. In
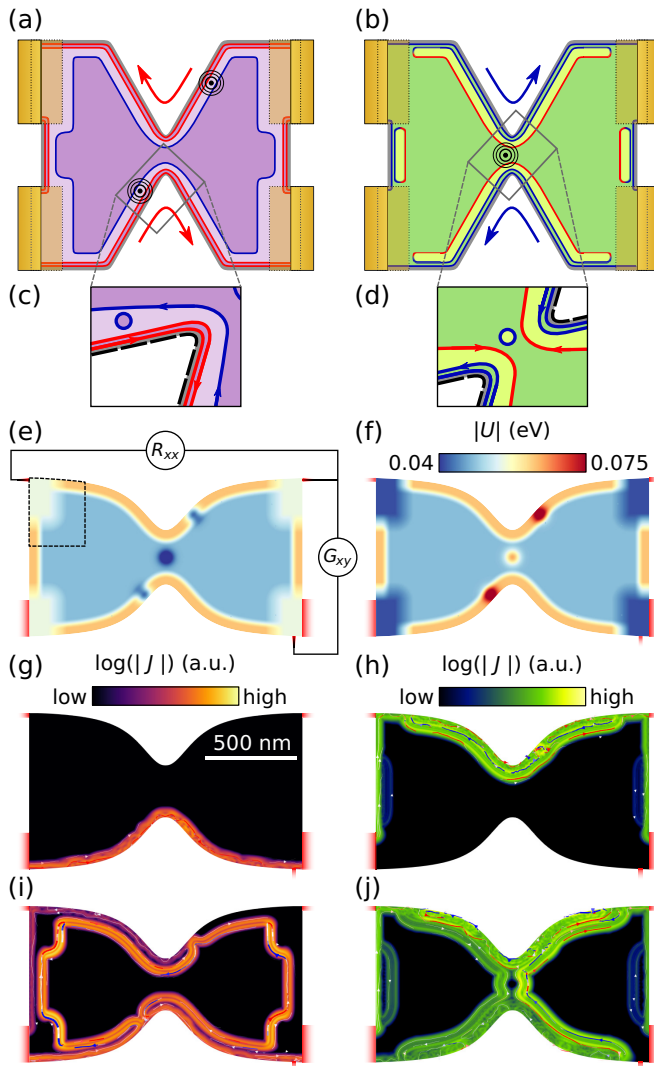
FIG. 4. (a) For holes, the inner QHEC describes a closed loop so that the effective filling factor is given by the light purple area's order (here $\nu = -6$). (b) For electrons, the inner (counterclockwise) QHEC forms a closed loop as it connects with the nearest clockwise QHEC so that the filling factor is given by the dark green area's order (here $\nu = 2$). (c) For holes, SGM signatures along the edges in Fig. 2(b) are caused by upstream QHECs coupling through an antidot located close to the constriction. (d) For electrons, coupling between opposite border QHECs via an antidot. (e, f) Potential landscapes of the simulated systems, with colors corresponding to the absolute value of the onsite potential landscape $|U|$, with the same parameters as in Figs. 3(h) and 3(i). (g–j) Current density maps obtained for holes with $V_{bg} = -4.8$ V (g), -3.8 V (i), and electrons with $V_{bg} = 6.4$ V (h), 7.8 V (j) as indicated with arrows in Fig. 5(a).

FIG. 5. (a) Simulated R_{xx} (plain line) and G_{xy} (dotted line) as a function of V_{bg} for a magnetic field $B = 4$ T. (b) Spatial configuration of the QHECs at the origin of the fluctuations in (a). (c) Spatial evolution of the potential (thick line) and of the three first LLs along the black dashed lines in (b). (d) Current density maps obtained from tight-binding calculations for $V_{bg} = 4.8$ V, as indicated with a red line in (a).

at a slightly different value of V_{bg} (calculated from E_F), so that holes flow through the inner QHEC loop, connecting both edges.

For electrons (right side of Fig. 4), the equilibrated QHECs form loops running along the edges, as illustrated in Fig. 4(b). Contrary to holes, the effective filling factor of the system is given by the bulk (here $\nu = 2$, in dark green), as for conventional semiconductor-based 2DEGs. The topological breakdown of QHECs can only be achieved by coupling the upstream QHECs of the upper and lower sides of the sample, which can only happen in the vicinity of the constriction, as illustrated with concentric black circles in Fig. 4(b). Electrons running along one of the edges (in a QHEC loop) can then be backscattered to the opposite side of the device. The SGM contrast highlighted at the center of the constriction in Figs. 2(c) and 2(d) is therefore the consequence of the coupling between the opposite QHECs loops through an antidot located at the center of the constriction, as depicted in Fig. 4(d) [22]. Simulations support this picture when introducing an antidot at the center of the constriction [Fig. 4(f)]. Figure 4(h) depicts a current density map where QHECs loops are visible along the edges, but the absence of coupling with the opposite edge prevents backscattering. When coupling is active [at different V_{bg}, as in Fig. 4(j)], electrons flow from one edge to the other through the central antidot and can be backscattered.

The simulated R_{xx} and G_{xy} curves as a function of V_{bg} (derived from the Fermi energy E_F), obtained in this system, are presented in Fig. 5(a) for holes (purple) and electrons (green). When R_{xx} is zero, the Hall conductivity exhibits the expected plateaus for graphene at $G_{xy} = 4(n + 1/2)e^2/h$, with n an integer. Nonzero R_{xx}, accompanied by the transition between two Hall plateaus, indicates the coupling between the opposite device edges due to the mechanisms discussed in Fig. 4 and the nonzero probability for charge carriers to be

particular, the coupling is achieved through an antidot, as depicted in Fig. 4(c) [10]. By introducing these antidots in the simulated potential landscape, with Gaussian functions centered close to the edges [see the potential map in Fig. 4(e)], we correctly capture the mechanism leading to holes backscattering. Figure 4(g) shows a simulated current density map where propagating QHECs are not coupled through the antidots. This is in stark contrast with Fig. 4(i) where coupling is achieved
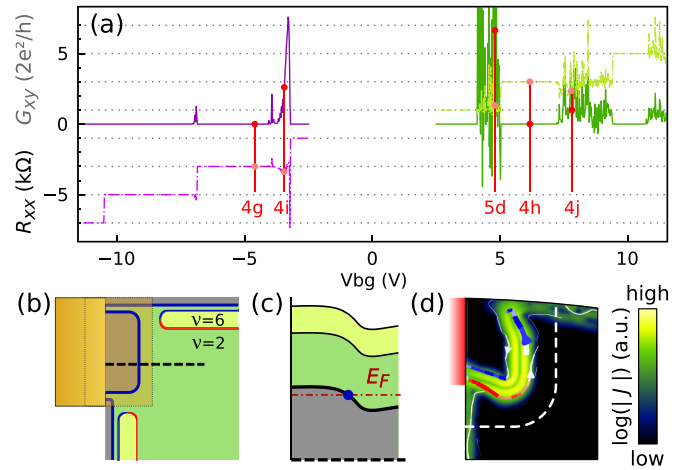
backscattered. The width of the transition between plateaus is governed by the latter coupling, so that in the experiment, with a larger amount of potential fluctuations, the nonzero-resistance transition region may obscure the signatures of the QH effect at integer-filling factor in the low B range. Nevertheless, the edge state picture is still valid in this regime, as shown in Figs. 4(i) and 4(j), corresponding to finite R_{xx}.

Another striking feature of the curve is the presence of large R_{xx} fluctuations on the electron side, similarly to the experimental data presented in Fig. 2(a). These fluctuations originate from extra QHECs running below the contacts, inducing a direct backscattering of charge carriers in the contact area [Figs. 5(b) and 5(c)]. This mechanism prevents a proper equilibration between the propagating QHECs and the contacts. In addition, current injection is strongly hampered in this situation, preventing proper determination of R_{xx}. Parasitic doping below the contacts, therefore, explains measurements artifacts such as the large variation of resistance even toward negative values reported here [Fig. 2(a)] as well as in previous experiments [19].

In summary, we have highlighted that line contacts, used for state-of-the-art encapsulated graphene samples, can lead to different spatial configurations of the upstream QHECs on the electron and hole sides. This yields distinct mechanisms at the origin of the QH topological breakdown for both charge carriers types. For holes, the breakdown occurs by coupling the upstream QHECs through antidots located at the device edges, whereas for electrons, all the QHECs running along the same edge are equilibrated and the breakdown occurs through the bulk, similar to conventional semiconductor 2DEGs. This interpretation provides a convincing explanation for microwave impedance microscopy results, where the QH topological breakdown was shown to coincide either with a conducting bulk, either with conducting edges, depending on the charge carriers type [6]. However, to strengthen the connection between theory and experiment, more extensive investigations are required, involving, e.g., different types of contact materials and a statistically significant number of studied devices. Nevertheless, our conclusions pinpoint the importance of considering the influence of contacts when designing 2D materials-based samples, in particular when these contacts are to be coupled with topologically protected edge channels.

[1] S. Komiyama and H. Hirai, Phys. Rev. B **40**, 7767 (1989).

[2] F. Dahlem, E. Ahlswede, J. Weis, and K. v. Klitzing, Phys. Rev. B **82**, 121305(R) (2010).

[3] J. Weis and K. von Klitzing, Phil. Trans. R. Soc. A **369**, 3954 (2011).

[4] L. Wang, I. Meric, P. Y. Huang, Q. Gao, Y. Gao, H. Tran, T. Taniguchi, K. Watanabe, L. M. Campos, D. A. Muller, J. Guo, P. Kim, J. Hone, K. L. Shepard, and C. R. Dean, Science **342**, 614 (2013).

[5] P. A. Khomyakov, A. A. Starikov, G. Brocks, and P. J. Kelly, Phys. Rev. B **82**, 115437 (2010).

[6] Y.-T. Cui, B. Wen, E. Y. Ma, G. Diankov, Z. Han, F. Amet, T. Taniguchi, K. Watanabe, D. Goldhaber-Gordon, C. R. Dean, and Z.-X. Shen, Phys. Rev. Lett. **117**, 186601 (2016).

[7] A. Nachawaty, M. Yang, S. Nanot, D. Kazazis, R. Yakimova, W. Escoffier, and B. Jouault, Phys. Rev. B **98**, 045403 (2018).

[8] A. Marguerite, J. Birkbeck, A. Aharon-Steinberg, D. Halbertal, K. Bagani, I. Marcus, Y. Myasoedov, A. K. Geim, D. J. Perello, and E. Zeldov, Nature (London) **575**, 628 (2019).

[9] A. Seredinski, A. W. Draelos, E. G. Arnault, M.-T. Wei, H. Li, T. Fleming, K. Watanabe, T. Taniguchi, F. Amet, and G. Finkelstein, Sci. Adv. **5**, eaaw8693 (2019).

[10] N. Moreau, B. Brun, S. Somanchi, K. Watanabe, T. Taniguchi, C. Stampfer, and B. Hackens, Nat. Commun. **12**, 4265 (2021).

[11] A. Aharon-Steinberg, A. Marguerite, D. J. Perello, K. Bagani, T. Holder, Y. Myasoedov, L. S. Levitov, A. K. Geim, and E. Zeldov, Nature (London) **593**, 528 (2021).

[12] P. G. Silvestrov and K. B. Efetov, Phys. Rev. B **77**, 155436 (2008).

[13] A. A. Shylau, I. V. Zozoulenko, H. Xu, and T. Heinzel, Phys. Rev. B **82**, 121410(R) (2010).

[14] S. Slizovskiy and V. I. Fal'ko, Phys. Rev. B **97**, 075404 (2018).

[15] J. M. Caridad, S. R. Power, A. A. Shylau, L. Gammelgaard, A.-P. Jauho, and P. Bøggild, Phys. Rev. B **99**, 195408 (2019).

[16] S. Kim, J. Schwenk, D. Walkup, Y. Zeng, F. Ghahari, S. T. Le, M. R. Slot, J. Berwanger, S. R. Blankenship, K. Watanabe, T. Taniguchi, F. J. Giessibl, N. B. Zhitenev, C. R. Dean, and J. A. Stroscio, Nat. Commun. **12**, 2852 (2021).

[17] B. Terrés, L. A. Chizhova, F. Libisch, J. Peiro, D. Jörger, S. Engels, A. Girschik, K. Watanabe, T. Taniguchi, S. V. Rotkin, J. Burgdörfer, and C. Stampfer, Nat. Commun. **7**, 11528 (2016).

[18] See Supplemental Material at http://link.aps.org/supplemental/10.1103/PhysRevB.104.L201406 for details about the experimental setup, filling factor obtained from a capacitance model, quantum Hall regime at low magnetic field, topological breakdown at different filling factors, impurity model, upstream modes with contacts modeled by ideal leads, doping induced by contacts and tight-binding simulations.

[19] F. Amet, A. J. Bestwick, J. R. Williams, L. Balicas, K. Watanabe, T. Taniguchi, and D. Goldhaber-Gordon, Nat. Commun. **6**, 5838 (2015).

[20] M. O. Goerbig, Rev. Mod. Phys. **83**, 1193 (2011).

[21] N. Paradiso, S. Heun, S. Roddaro, D. Venturelli, F. Taddei, V. Giovannetti, R. Fazio, G. Biasiol, L. Sorba, and F. Beltram, Phys. Rev. B **83**, 155305 (2011).

[22] B. Hackens, F. Martins, S. Faniel, C. Dutu, H. Sellier, S. Huant, M. Pala, L. Desplanque, X. Wallart, and V. Bayot, Nat. Commun. **1**, 39 (2010).

[23] F. Martins, S. Faniel, B. Rosenow, H. Sellier, S. Huant, M. G. Pala, L. Desplanque, X. Wallart, V. Bayot, and B. Hackens, Sci. Rep. **3**, 1416 (2013).

[24] N. Pascher, C. Rössler, T. Ihn, K. Ensslin, C. Reichl, and W. Wegscheider, Phys. Rev. X **4**, 011014 (2014).

[25] G. Giovannetti, P. A. Khomyakov, G. Brocks, V. M. Karpan, J. van den Brink, and P. J. Kelly, Phys. Rev. Lett. **101**, 026803 (2008).

[26] F. A. Chaves, D. Jiménez, A. W. Cummings, and S. Roche, J. Appl. Phys. **115**, 164513 (2014).

[27] J. R. Waldrop, J. Vac. Sci. Technol. B **2**, 445 (1984).

[28] L. Gao, J. Souto-Casares, J. R. Chelikowsky, and A. A. Demkov, J. Chem. Phys. **147**, 214301 (2017).

[29] H. Z. Jooya, X. Fan, K. S. McKay, D. P. Pappas, D. A. Hite, and H. R. Sadeghpour, Mol. Phys. **117**, 2157 (2019).

[30] C. W. Groth, M. Wimmer, R. A. Akhmerov, and X. Waintal, New J. Phys. **16**, 063065 (2014).

[31] M.-H. Liu, P. Rickhaus, P. Makk, E. Tóvári, R. Maurand, F. Tkatschenko, M. Weiss, C. Schönenberger, and K. Richter, Phys. Rev. Lett. **114**, 036601 (2015).